Petroleum Science 21 (2024) 4204–4218

Contents lists available at ScienceDirect

Petroleum Science

journal homepage: www.keaipublishing.com/en/journals/petroleum-science

Original Paper

# Evaluation of SC-$CO_2$–brine on the micro-mechanical properties of lamina shales by micro-scratch test

Liu Yang [a, b, 1], Zhao-Yang Liu [a, b, 1], Yuan-Xun Nie [c, *], Zhen-Chuan Han [a, b], Fei Gong [a, b], Ming-Jun Li [a, b], Yan Liu [a, b]

[a] State Key Laboratory for Tunnel Engineering, China University of Mining & Technology (Beijing), Beijing, 100083, China
[b] School of Mechanics and Civil Engineering, China University of Mining and Technology (Beijing), Beijing, 100083, China
[c] Department of Hydraulic Engineering, State Key Laboratory of Hydro science and Engineering, Tsinghua University, Beijing, 100084, China

ARTICLE INFO

*Article history:*
Received 29 February 2024
Received in revised form
15 July 2024
Accepted 16 July 2024
Available online 18 July 2024

Edited by Yan-Hua Sun

*Keywords:*
Lamina shale
SC-$CO_2$–brine–rock interaction
Micro-scratch test
Micro-mechanical properties
Elastic-plastic failure mechanism

ABSTRACT

The mechanism of SC-$CO_2$–brine–rock interaction (SCBRI) and its effect on the mechanical properties of shale are crucial for shale oil development and $CO_2$ sequestration. To clarify the influence of SCBRI on the micromechanics of shale, the lamina and matrix of shale were saturated with SC-$CO_2$–brine for 2, 4, 6, and 8 days, respectively. The micro-scratch technique was then used to measure the localized fracture toughness before and after SC-$CO_2$–brine saturation. Combining the micro-scratch results with SEM-QEMSCAN-EDS analysis, the differences in mineral composition and mechanical properties of lamina (primarily composed of carbonate minerals) and matrix (primarily composed of clay minerals) were studied. The QEMSCAN analysis and micro-scratch results indicate distinct mineralogical compositions and mechanical properties between the lamina and the matrix. The results showed that: (1) SCBRI leads to the decrease in carbonate mineral content and the significant increase in matrix porosity and laminar cracks. In addition, the damage degree increased at saturation for 6 days. (2) SCBRI weakens the mechanical properties of shale. The scratch depth of laminar and matrix increased by 34.38% and 1.02%, and the fracture toughness decreased by 34.38% and 13.11%. It showed a trend of first increasing and then decreasing. (3) SCBRI enhances the plastic deformation behavior of shale, and the plastic index of lamina and matrix increases by 18.75% and 21.58%, respectively. These results are of great significance for evaluating the mechanical properties of shale oil and gas extraction by $CO_2$.


## 1. Introduction

The exploration and production of unconventional oil and gas resources, particularly shale oil, have gained significant importance due to the increasing global demand for energy (Li et al., 2018). Currently, hydraulic fracturing has become the primary technique for the exploitation of shale reservoirs (Yang L. et al., 2023). However, this technique requires a substantial volume of water resources, which raises environmental concerns (Osborn et al., 2011). To reduce the environmental impact of energy production, the research of waterless fracturing technique has become a critical focus in the contemporary energy sector (Middleton et al., 2014). Due to its numerous benefits in enhancing fracture complexity and restoring formation energy, the carbon dioxide ($CO_2$) fracturing has been emerged as a very promising method (Tan et al., 2022). Under reservoir conditions, $CO_2$ remains a supercritical state known as SC-$CO_2$, which exhibits unique properties such as high density, high diffusivity, low viscosity and very low surface tension (Zhou et al., 2021). The low surface tension of SC-$CO_2$ facilitates its penetration into fractures and pores. Consequently, there exists a strong probability that the injected carbon dioxide ($CO_2$) dissolves into the formation brine, leading to a mildly acidic milieu. This, in turn, can induce alterations in both the physical and chemical characteristics of the shale reservoirs (Stavropoulou and Laloui, 2022). Laminated shale contains its unique distribution of rock layers and textural features along the vertical direction (Heng et al., 2020). The presence of lamina and non-homogeneous mechanical properties of different rock minerals induce difficulties in the development of shale oil. Therefore, it is important to investigate the mechanism of

* Corresponding author.
*E-mail address:* nieyuanxun@126.com (Y.-X. Nie).
[1] Liu Yang and Zhao-Yang Liu are co-first authors of the article.

https://doi.org/10.1016/j.petsci.2024.07.017

the interactions between SC-$CO_2$–brine and laminated shale, as well as the impact of these interactions on the alteration of mechanical properties of shales.

The SC-$CO_2$–brine-rock interaction (SCBRI) in shale is a complex process, primarily due to the reversible ionization of carbonic acid and the dependence of $CO_2$ solubility on temperature and pressure. These factors play a significant role in governing the physico-chemical reactions between these media (Zhang et al., 2017). When $CO_2$ dissolves into the reservoir brine, it ionize $H^+$, leading to the dissolution or precipitation of various components in the shale, such as carbonate, clay, and organic minerals (Espinoza et al., 2011). The dissolution of carbonate is often more pronounced compared to that of quartz (Goodman et al., 2019). Simultaneously, these chemical interactions induce changes in the pore structure of the shale (Luo et al., 2019), resulting in the increases in porosity and permeability (Tao et al., 2022). In addition, the mechanical properties of shale are also influenced by alterations in minerals content and pore space. Previous research has demonstrated that the tensile strength, compressive strength, and Young's modulus of shale exhibit a decrease trend, while Poisson's ratio increases due to the SC-$CO_2$ saturation (Bai et al., 2021). There is a positive correlation between the reduction of mechanical parameters (including tensile strength, compressive strength and fracture toughness) and the saturation pressure (Yang K. et al., 2023). Presently, most research has investigated the changes in macroscopic mechanical properties of shale. However, during the $CO_2$ storage process, it is worth noting that the fracture initiation and the changes of mechanical properties exhibit a strong correlation with the microscale mechanical properties of rocks.

In recent years, the application of nanotechnology has led to the emergence of the nanoindentation testing technique as a valuable method to assess micromechanical properties of materials (Liu et al., 2023). Nanoindentation technique has been widely used in the investigation of many geological materials that exhibit heterogeneous characteristics, such as granite (Golovin et al., 2018), marble (Bandini et al., 2014), shale (Fan et al., 2019), and coal (Liu A. et al., 2022). Shi et al. (2020) used nanoindentation to investigate the influence of SCBRI on the specimens, and the results indicated that the SCBRI led to a reduction in both hardness and Young's modulus. Notably, the magnitude of this effect was seen to be comparatively lower for quartz than clay. Liu et al. (2023b) found that the creep deformation of quartz and organic matter after SC-$CO_2$–brine saturation reached 1.81 and 1.42 times of the initial creep deformation by the nanoindentation technique. However, nanoindentation requires numerous indentation points to obtain accurate mechanical properties, which requires a significant investment of time and effort (Yang et al., 2024). In contrast, the micro-scratch technique enables the continuous assessment of material mechanical characteristics and facilitates the acquisition of a substantial volume of data points within a short time. Richard et al. (2012) established a connection between the uniaxial compression strengths acquired through scratch tests and that obtained from the standard uniaxial compression studies. The study conducted by Wei et al. (2021) investigated the deformation and fracture toughness of cementite under scratching conditions. Akono et al. (2011) conducted some micro-scratch tests on several materials, and established the equation to determine the fracture toughness. Although previous studies have studied the SCBRIs on rocks through micro-indentation and macroscopic tests, there is a lack of investigation into the influence of SC-$CO_2$–brine on the microscopic mechanical characteristics of laminated shales using micro-scratching techniques.

In this paper, the laminated shale of the Lower Cretaceous Qingshankou Formation in the northern of the Songliao Basin is studied. The effects of SCBRI on the microstructure, damage failure mode, scratch depth, and fracture toughness of the shale lamina and matrix were studied using micro-scratch and QEMSCAN-SEM-EDS scanning techniques. Firstly, under reservoir temperature and pressure, SC-$CO_2$–brine saturation experiments were carried out to make the shale fully contacts with $CO_2$. Secondly, QEMSCAN-SEM tests were used to investigate the influence of SCBRI on the mineral changes and microstructure of the lamina and matrix. Finally, the influence of SCBRI on the micro-damage failure mechanism, scratch depth, and fracture toughness of the lamina and matrix was investigated by micro-scratch technique. This study provides direct mechanical measurements of the mineral constituents in the treated lamina and matrix, offering an insight into the SCBRI from a microscopic perspective.

## 2. Material and methods

### 2.1. Specimen preparation

The terrestrial lake basins in China exhibit complex geological characteristics, with significant variations in depositional settings and diagenesis. As a consequence, the sedimentary rocks in these basins are highly heterogeneous, and their laminated structure plays an important role in fracture propagation. The samples shown in Fig. 1 were cut from a reservoir core of laminated shale in the Lower Cretaceous Qingshankou Formation of the northern Songliao Basin, China. The thickness of the lamina is less than 0.5 mm, and the sample sizes were 10 mm × 10 mm × 5 mm (Li et al., 2022). To avoid any structural damage during sample preparation, the shale specimens were mounted in epoxy resin (placed in a mold and the resin is poured over it) and left overnight to allow the resin to solidify. By curing the epoxy resin, its stress damage is minimized during the cutting process (Veytskin et al., 2017). Furthermore, to ensure the surface smoothness and flatness required for the nano-scratch tests, the sample surfaces were first roughly polished using sandpaper, followed by a more precise polishing process using an argon ion polisher. The shale samples were carefully managed to maintain a root-mean-square (RMS) roughness ranging from 120 to 150 nm (Liu Y. et al., 2022).

### 2.2. SC-$CO_2$–brine saturation process

The $CO_2$–brine saturation procedure is shown in Fig. 2. To avoid clay swelling and simulate the in-situ groundwater conditions, a brine solution was made by dissolving 2 wt% NaCl and 1 wt% KCl in deionized water (Nie et al., 2022). As shown in Fig. 2, the shale sample was placed on a reaction table within a vacuum vessel. Brine was subsequently pumped into the vessel, after which $CO_2$ was injected into the vessel until the pressure reached 15 MPa. The temperature of the entire $CO_2$–brine saturation system was maintained at 70 °C using a water bath system. These experimental conditions exceed the critical temperature and pressure of supercritical carbon dioxide (SC-$CO_2$), keeping $CO_2$ in the supercritical phase (Fatah et al., 2021). The pressure in the reaction vessel was continuously monitored using a pressure sensor. To study the influence of time on the interactions between SC-$CO_2$–brine and shale, the saturation time was designed to 2, 4, 6 and 8 days, after which micro-scratch tests were conducted. To minimize the impact of ambient air exposure, the nano-scratch tests were performed within 6 h after the samples removed from the vessel.

The experimental flow chart is shown in Fig. 3. The spectroscopic probe of the QEMSCAN instrument is used to detect characteristic X-ray signals, which enabled the identification of elemental information at specific locations within the samples. The

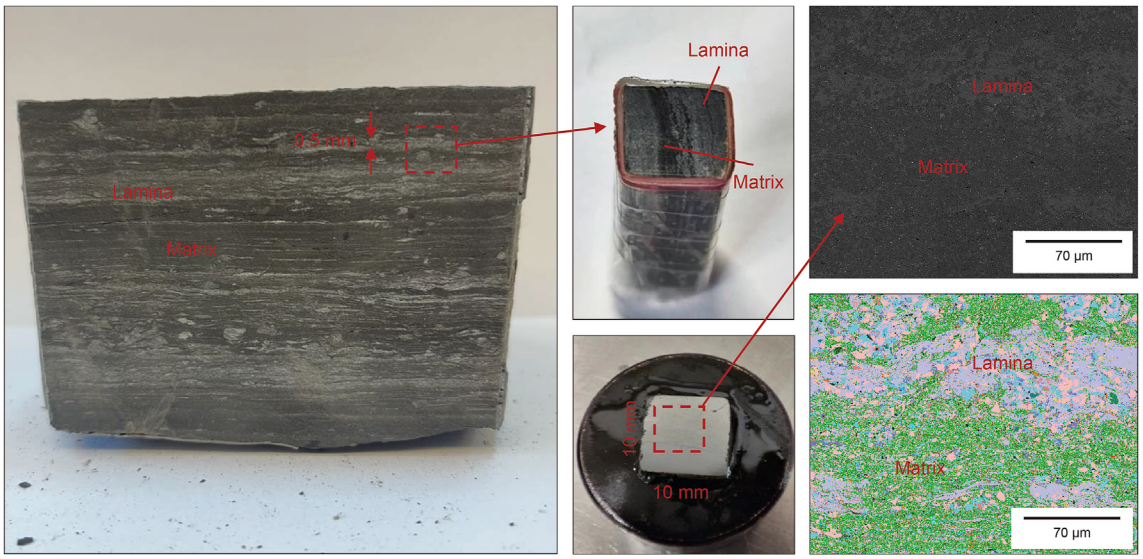


**Fig. 1.** Schematic diagram of laminated samples.

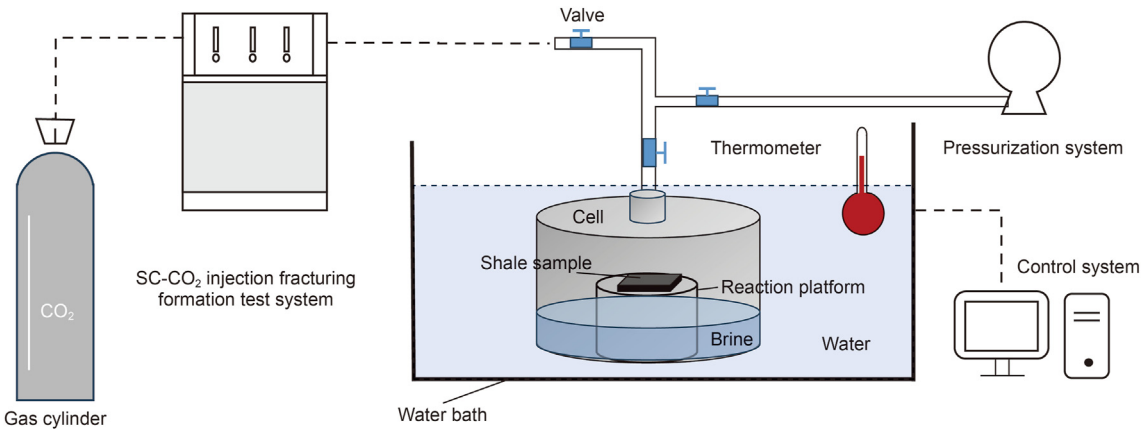


**Fig. 2.** Schematic of the SC-$CO_2$–brine treatment process on shale samples.

QEMSCAN analysis provided the information of mineral composition and distribution within the lamina and matrix. Subsequently, scanning electron microscopy (SEM) was used to detect the microstructure of the shale lamina and matrix. In order to reduce the deviation of the experiment caused by the heterogeneity of shale, the area with relatively homogeneous QEMSCAN and SEM scanning results is selected for the experiment.

Then, micro-scratch technique was used to selectively scratch the lamina and matrix at various saturation time. SEM was further used to observe the location and morphology of the scratches. After each saturation time, SEM was again used to detect the any alterations occurring on the locations of the scratches. Finally, upon completion of the final scratch, the QEMSCAN-SEM-EDS technique was used once more to examine the influence of SC-$CO_2$ on the shale lamina and matrix. In addition, in order to avoid the residual stress and stress concentration after the scratch test, the scratch spacing under different saturation time is about 60 μm. The spacing between the scratches is much larger than the maximum scratch depth of 3 μm, which can greatly reduce the stress effect between adjacent scratches.

### 2.3. Nano-scratching test

As shown in Fig. 4(a), the Berkovich probe was used for the micro-scratch test conducted in the KEYSIGHT G200. The schematic diagram of indenter model is shown in Fig. 4(b). The angle $\alpha$ between the prism and the center line is 65.3°, while the angle $\beta$ between the lateral prism and the center line is 70.05°. Fig. 4(c) shows the side perspective of the Bohrer indenter during the scratching process. At the initial stage of the scratch process, the indenter was applied onto the sample with a constant vertical force ($F_V$) of 100 mN. Meanwhile, a horizontal force applied on the surface of the sample thorough the probe, with a constant velocity ($V_T$) of 30 μm/s. In this study, the variable $d$ and $L$ denote the scratch depth and length, respectively. Fig. 4(d) shows the frontal view of the micro-scratch process, where $A(d)$ and $p(d)$ denote the projected area of the plane in the direction of indentation and the side length of the projected area, respectively (Nie et al., 2024).

The micro-scratch technique enables to assess the microfracture characteristics of shale with a high precision (Liu et al., 2023a). The fracture toughness ($K_{IC}$) refers to the capacity of a material to resist

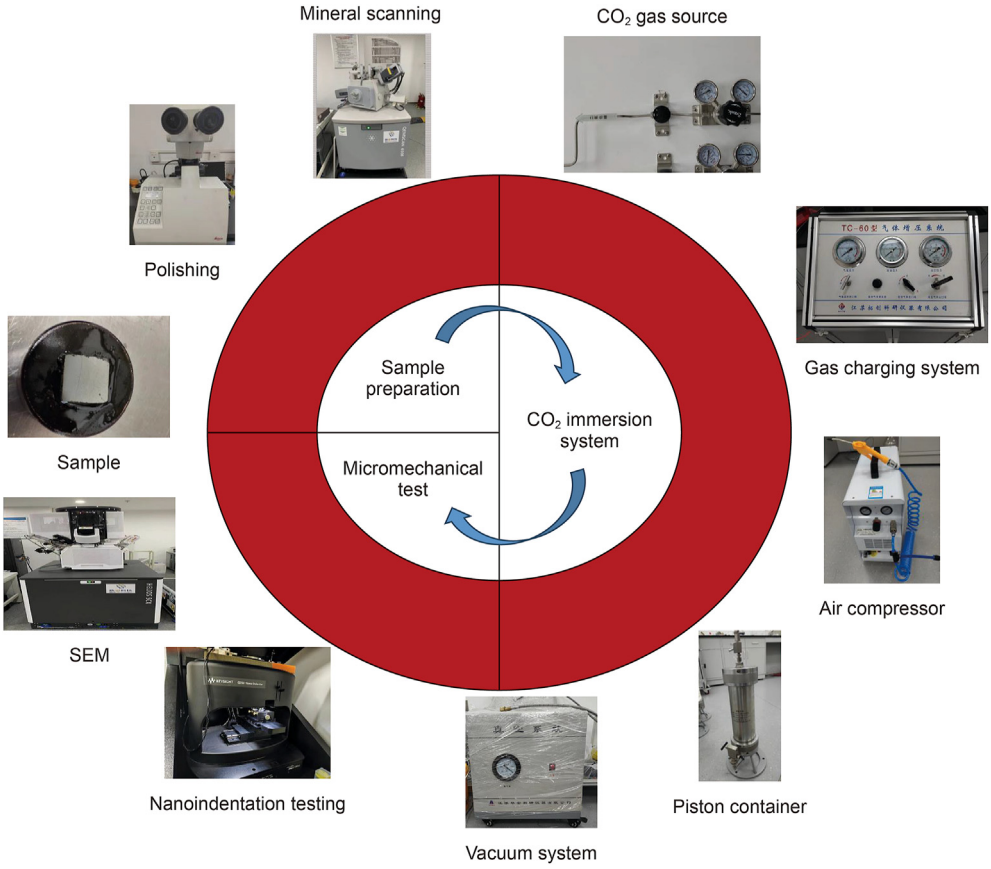


**Fig. 3.** Experimental flow chart.

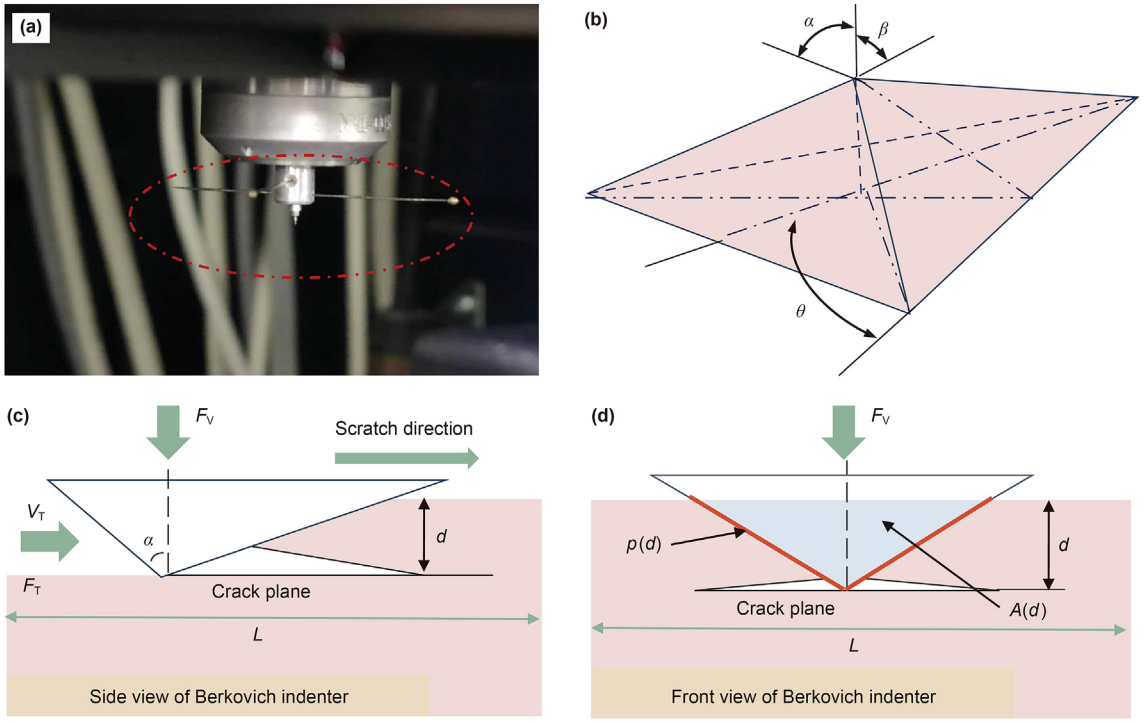


**Fig. 4.** Micro-scratch modelling. (**a**) G200 nano-probe; (**b**) Schematic diagram of the probe; (**c**) Side view of the micro-scratch process; (**d**) Front view of the micro-scratch process.

fracture initiation when it is exposed to external load. The $K_{IC}$ of a micro-scratch can be determined using the follow equations (Akono and Kabir, 2016):

$$K_{IC} = \frac{F_T}{\sqrt{2p(d)A(d)}} \tag{1}$$

$$A(d) = \tan\theta \times [\tan\alpha + \tan\beta] \times d^2 \tag{2}$$

$$p(d) = d \times \sqrt{1 + \tan\theta \times (\tan\alpha + \tan\beta)} \tag{3}$$

where $F_T$ is the horizontal force; and $d$ is the depth of the scratch. For the Berkovich probe tip, $A(d)$ is proportional to $d^2$ and $p(d)$. $A(d)$ is proportional to $d^3$ (Akono and Ulm, 2017). The angle $\theta$, which corresponds to the specific orientation of the Berkovich probe used in the nano-scratch test, is 30° (Wei et al., 2021).

## 3. Results and discussion

### 3.1. Mineralogical effects of SCBRI on shales

The content and distribution of different minerals in shale were determined using QEMSCAN, as shown in Fig. 5. The primary minerals in the samples include illite, quartz, calcite, albite, dolomite, muscovite, apatite, and pyrite.

As shown in Eq. (4), $CO_2$ dissolves into the brine, ionizing $H^+$. The chemical reactions between calcite, albite, illite, quartz in shale and $H^+$ are represented by Eqs. (5)–(8) (Cheng et al., 2020).

$$CO_2 + H_2O \rightleftharpoons H^+ + HCO_3^- \rightleftharpoons 2H^+ + CO_3^{2-} \tag{4}$$

$$\text{Calcite} + 2H^+ \rightleftharpoons Ca^{2+} + CO_2 + H_2O \tag{5}$$

$$\text{Illite} + 1.1H^+ \rightleftharpoons 0.77\text{kaolinite} + 0.6K^+ + 0.25Mg^{2+} + 1.2\text{quartz} + 1.35H_2O \tag{6}$$

$$\text{Albite} + 4H_2O + 4CO_2 \rightleftharpoons 2Na^+ + 2HCO_3^- + Al_2Si_2O_5(OH)_4 \tag{7}$$

$$\text{Quartz}: SiO_2 + 2H_2O \rightleftharpoons H_2SiO_4 \tag{8}$$

$$\text{Quartz} + 2OH^- \rightleftharpoons SiO_3^{2-} + H_2O \tag{9}$$

Variations in mineral type and content lead to different degrees of chemical reaction. The mineral content in the matrix is 43.94% illite, 25.20% quartz, 12.36% albite, and 6.26% calcite. The content of the lamina is comprised of 59.93% calcite, 16.58% quartz, 6.27% illite, and 8.83% albite. In addition, the matrix and lamina also contain a

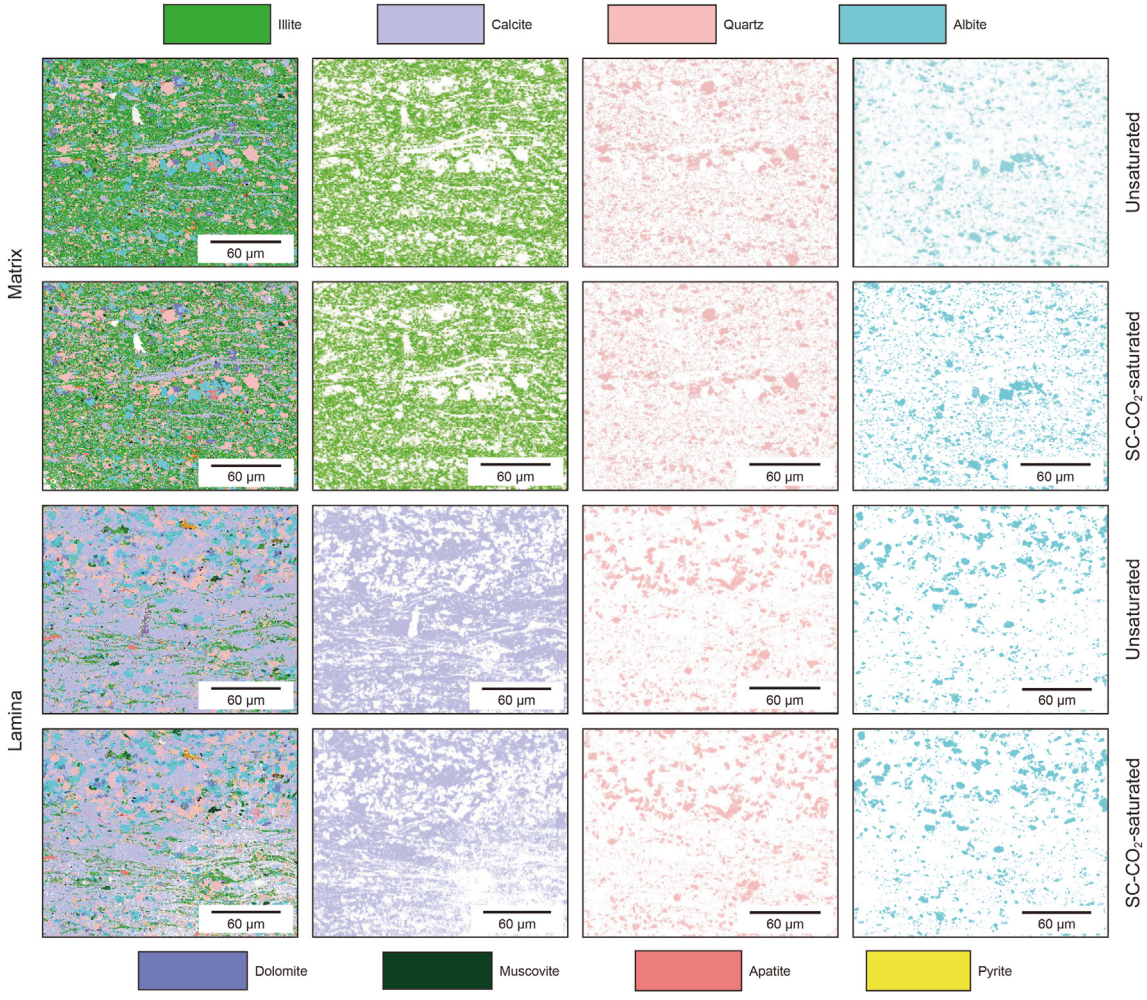


**Fig. 5.** Mineral distribution in shale determined using QEMSCAN.

small amount of dolomite, muscovite, apatite, pyrite, and other minerals, the total content is about 10%. Because these minerals make up very little of the shale, the reaction of these minerals with $CO_2$ was not considered in this study.

The effect of SCBRIs on minerals depends on the specific mineral species. The changes in mineral composition within the matrix before and after SC-$CO_2$–brine saturation are shown in Fig. 6(a). After the chemical interactions between SC-$CO_2$–brine and the matrix, the mineral content exhibited several changes. There was a decrease in the content of calcite, albite, and clay by 0.25%, 0.20%, and 0.04%, respectively. Conversely, the quartz content increased by 2.32%. These observed variations in matrix mineral distribution and content suggest a limited degree of interaction between SC-$CO_2$–brine and the clay minerals within the matrix. The increase in quartz content within the matrix can be partially attributed to the limited generation of quartz during the dissolution of illite. This phenomenon results in an augmentation of quartz content. Alternatively, the observed increase in quartz concentration can also be attributed to the concurrent decrease in clay and carbonate mineral contents.

Fig. 6(b) shows the observed alterations in the mineral composition within the lamina before and after SC-$CO_2$–brine saturation. The data reveals a 15% reduction in the calcite content, accompanied by a 0.74% increase in clay content and a 0.69% increase in albite content within the lamina after the saturation process. The substantial decrease in calcite content indicates a more pronounced chemical reaction between the SC-$CO_2$–brine and the lamina. This reduction in calcite content can be attributed to the dissolution induced by SCBRI. SC-$CO_2$ dissolves in brine to form a carbonic acid solution, which enters the rock interior through pores and natural fractures. As shown in Eq. (5), the $H^+$ of the carbonate solution permeates the mineral lattice structure and reacts with the ions in it. This reaction causes the calcite mineral to gradually dissolve and release its cations (Wang et al., 2013). The chemical interaction between minerals and the SC-$CO_2$–brine is a multifaceted and protracted evolutionary process, which warrants further research to comprehensively understand the long-term mechanism of mineral trapping.

### 3.2. The influence of SCBRI on microstructure

The scratching process alters the initial micro-morphology on the surfaces of shale, leading to the formation of scratch grooves accompanied by changes in pore structure and the development of micro-fractures. These fractures, extending through the entire thickness of the rock, are commonly referred to as “through-thickness fracturing” (Bull, 1997). The mode of failure that arises between the area of the groove and the adjacent minerals is known as the interfacial failure mode.

Fig. 7(a) shows the scratch pattern in the matrix area before the SCBRI, with the scratch direction from bottom to top. The yellow striped areas represent the grooves formed by the scratches penetrating into the matrix at specific depths. The fracture damage pattern observed in the matrix grooves is attributed to the relatively low bond strength among the clay particles. The thickness-through fractures in the matrix are plastic fractures with a high density, primarily in the form of fine flexural fractures. The red band shows the damage zones at the interface between the matrix grooves and the surrounding minerals. Plastic deformation and shear damage are observed in these damage zones. The scratched interface exhibits morphological features of wavy edges and mineral flaking. These observed phenomena can be attributed to the stress concentration resulting from the scratch-induced interaction between the grooves and the adjacent minerals.

The surface of the matrix after 2 days of saturation is shown in Fig. 7(b). Some of the minerals in the scratch grooves are displaced and transported, and some new pores create. There is little change observed outside the scratch grooves. The surface of the matrix after 4 days of saturation is shown in Fig. 7(c). A small number of flocculent crystals appear in the scratch grooves, and the number of pores increases. Fig. 7(e) and (f) shows the surface of the matrix after 6 and 8 days of saturation, respectively. The flocculent crystals in the scratch grooves develop into granular crystals, accompanied by the formation of new pores. Some of the newly emerging mineral particles in the grooves can block part of the pore space. The EDS spectra of the granular crystals are shown in Fig. 7(g) and (h). These analyses indicate a significant proportion of Ca ions, suggesting that the crystals are primarily composed of calcium carbonate. Additionally, some new minerals appear outside of the scratch grooves. The emergence of these new minerals can be attributed to two factors: the dissolution of shallow minerals, leading to the emergence of deep minerals and the migration of SCBRI. As shown in Fig. 7(f), the minerals in the lower right region are significantly dissolved under the influence of SCBRI, resulting in the formation of broken mineral particles. Furthermore, as shown in Fig. 7(f), some of the new crystal particles disappear due to the migration of SCBRI.

Fig. 8(a) shows the scratch at the lamina area before SC-$CO_2$–brine saturation. Through-thickness fractures in the lamina are curved and directionally oriented. The angles between these

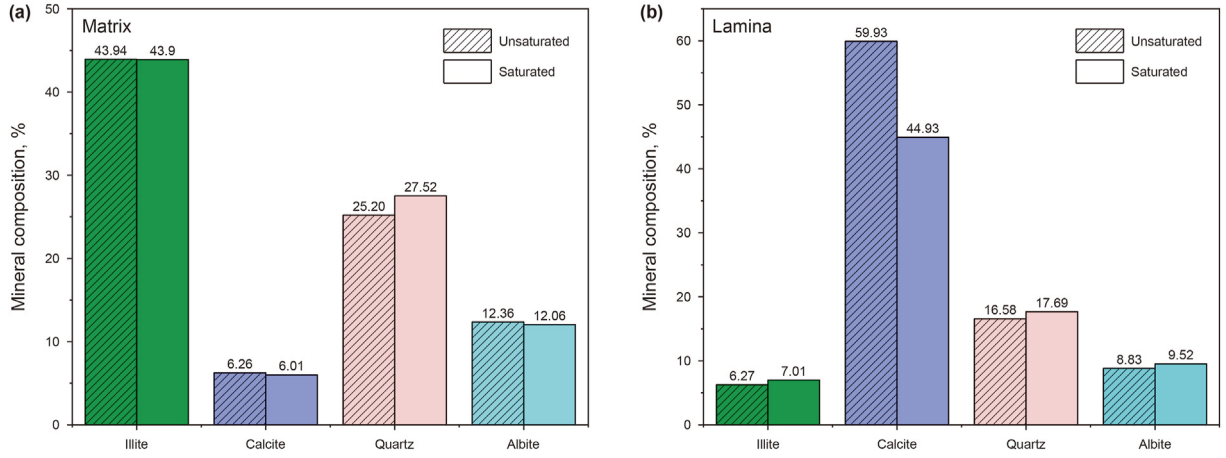


**Fig. 6.** Changes in mineral composition in shale before and after SC-$CO_2$–brine saturation. (**a**) Matrix; (**b**) Lamina.

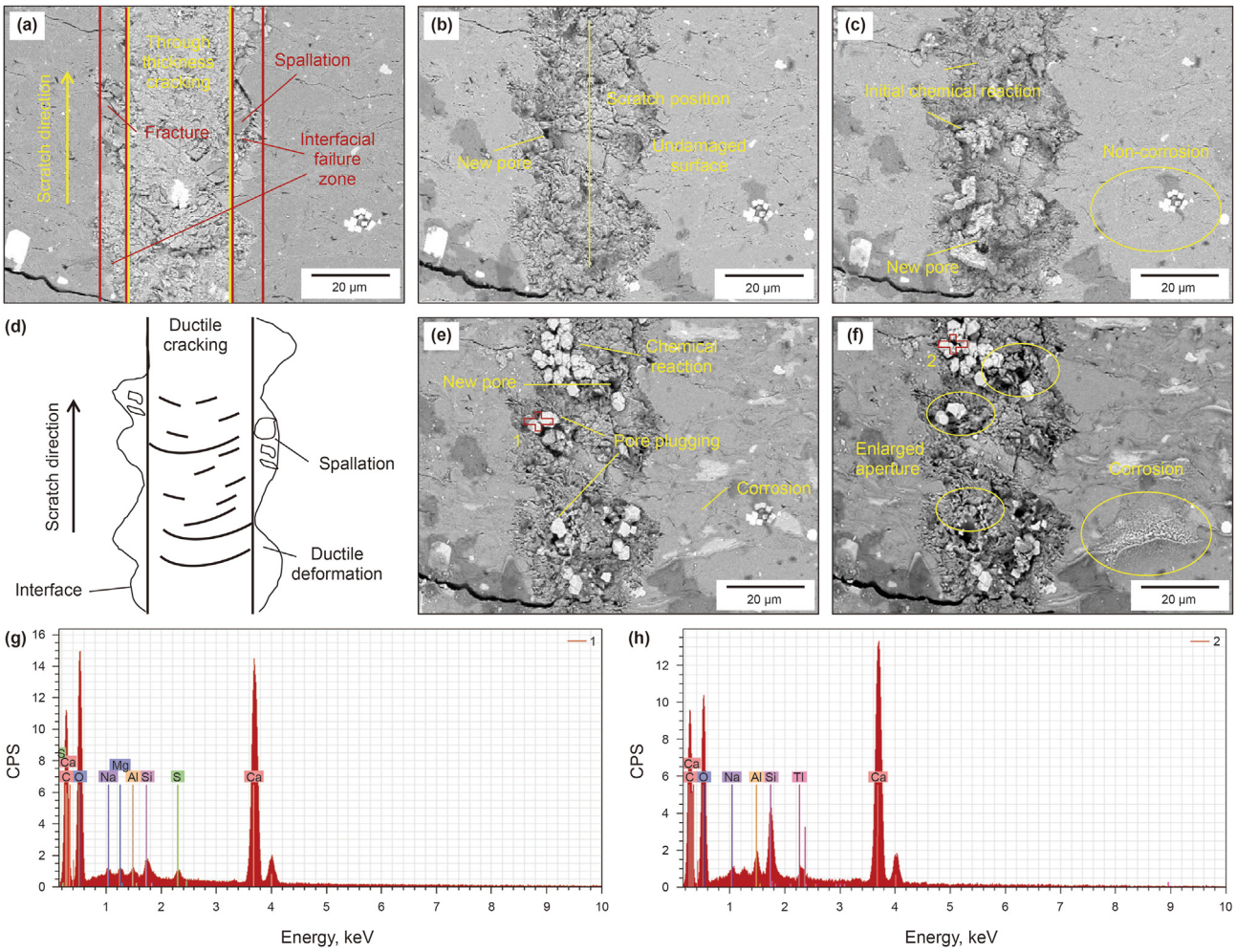


**Fig. 7.** SEM images of scratching at the same position of the matrix after 0 (**a**), 2 (**b**), 4 (**c**), 6 (**e**), and 8 (**f**) days of saturation. (**d**) Matrix damage pattern. EDS results of point 1 (**g**) and point 2 (**h**).

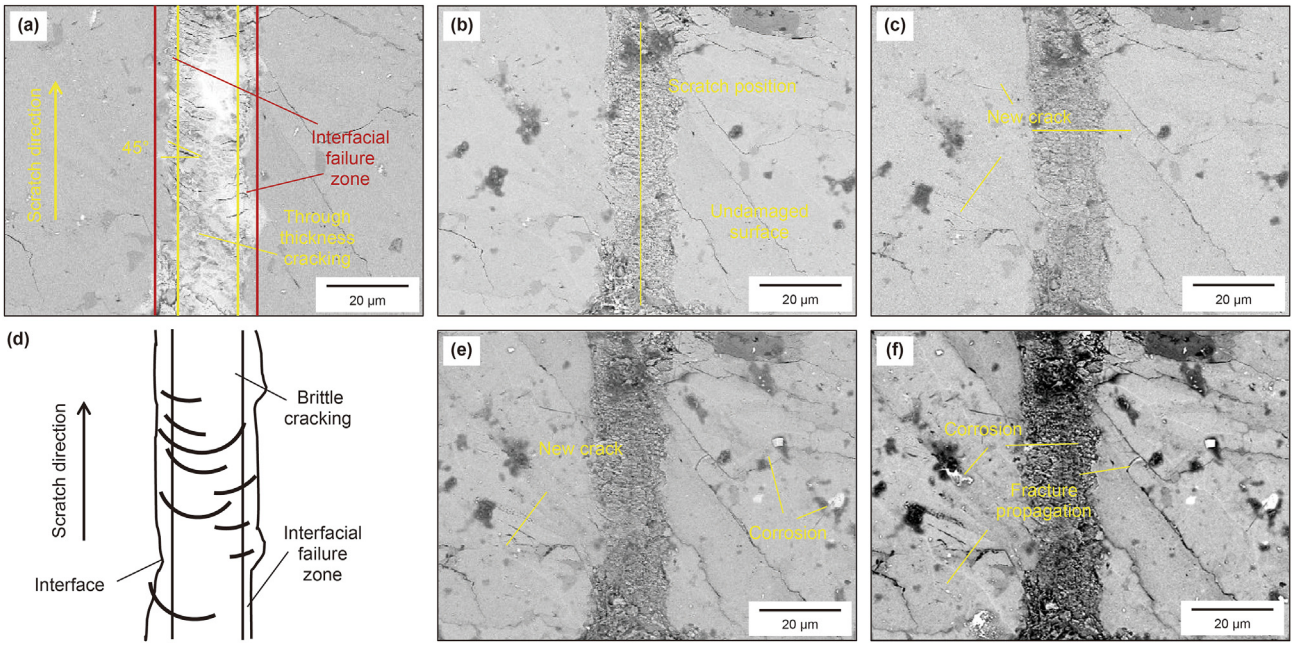


**Fig. 8.** SEM images of the same scratch at the lamina after 0 (**a**), 2 (**b**), 4 (**c**), 6 (**e**), 8 (**f**) days of saturation. (**d**) Laminate damage pattern.

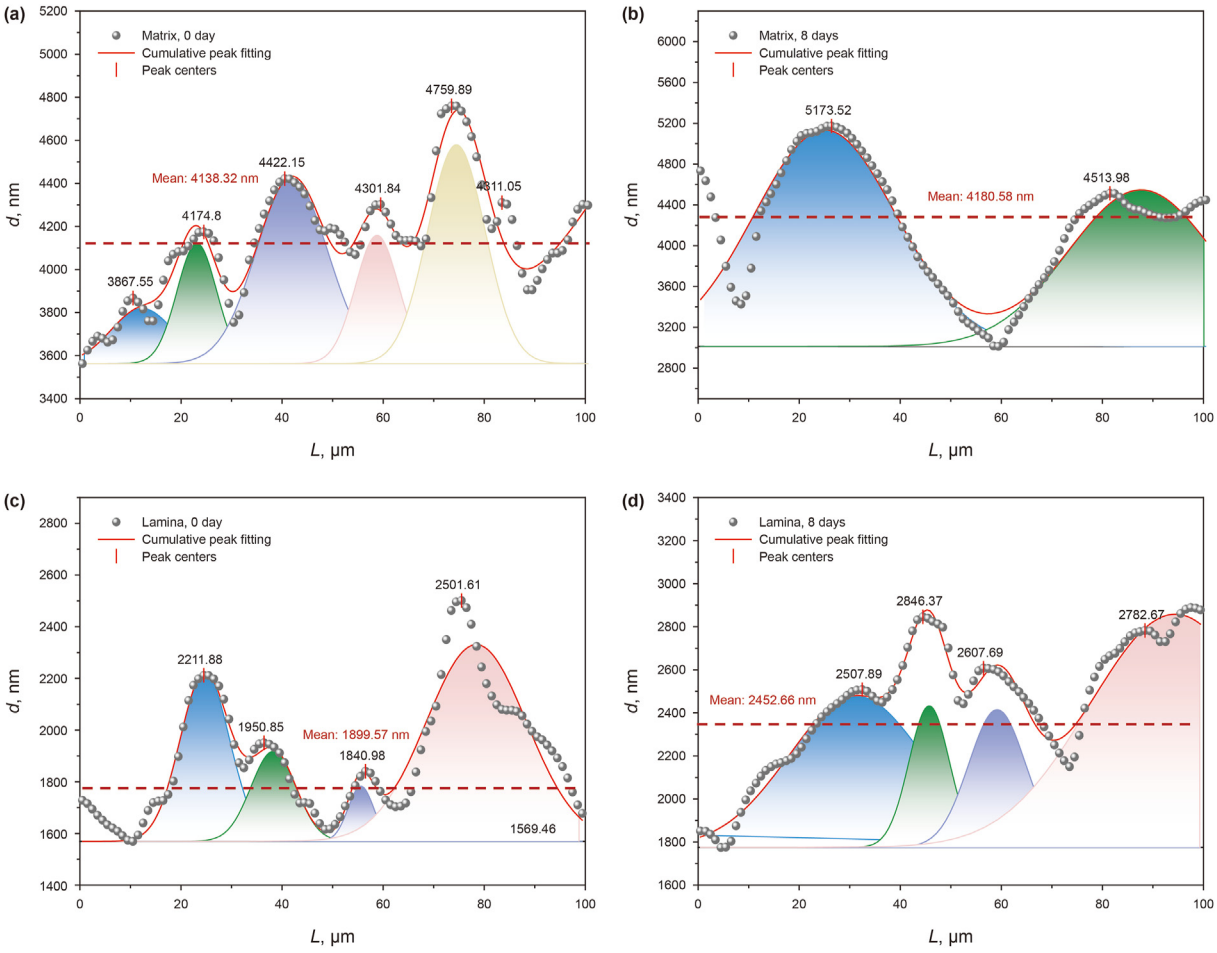


**Fig. 9.** Morphological characteristics of the scratch depth–displacement curves for matrix and lamina. (**a**) Matrix, 0 day; (**b**) Matrix, 8 days; (**c**) Lamina, 0 day; (**d**) Lamina, 8 days.

fractures and the scratch grooves are approximately 45°. These are yield fractures resulting from shear damage. After the yield damage, the fractures extend to the edge of the scratch interface. In addition, the scratch interface is smooth and straight, with no evidence of mineral stripping.

Fig. 8(b) shows the surface of the lamina after 2 days of saturation. Some of the minerals in the scratch grooves are displaced and transported, and some new pores create. The surface of the lamina after 4 days of saturation is shown in Fig. 8(c). Many microcracks is observed outside the scratch grooves. Fig. 8(e) and (f) shows the surface of the lamina after 6 and 8 days of saturation, respectively. The surface of the sample is significantly altered, with the appearance of a large number of interconnected microcracks. The microcracks within the scratch grooves have been dissolved and transported, forming a network of interconnected granular bands.

In summary, SCBRI has a significant influence on the microstructure of shale. Within the matrix, the number and size of pores increases significantly after saturation. Similarly, the lamina exhibits a significant increase in the number and size of microcracks after saturation. This can be attributed to the ultra-low interfacial tension and viscosity of SC-$CO_2$, which facilitates its penetration into the shale micropores and thin layers (Wu et al., 2022). As a result, the SC-$CO_2$ tends to adsorb equilibrium where fractures and pores develop. Moreover, the extent of the effect of SCBRI on shale is influenced by time. During the first 4 days of saturation, the changes in pores and minerals within the lamina and matrix are small. However, by the 6th and 8th day after saturation, the surface changes in the shale are pronounced, with the development of observable pores in the lamina and matrix, an increase number of cracks, and increase transport and chemical reaction of minerals. In addition, the presence of calcite in the matrix grooves indicates that the process of SC-$CO_2$–brine dissolution of calcite is a dynamic process in which dissolution and precipitation coexist. However, the dissolution and newly formed precipitation are spatially heterogeneous (Lu et al., 2016). There is a certain degree of chemical inhomogeneity on the rock surface due to the difference of mineral inhomogeneity and the fluctuation of the scratch damage surface. As a result, the overall effects of SCBRI on mineral reactions and pore networks will be more complex and require further study.

### 3.3. Deformation during the loading and holding process

When the indenter applies pressure to the material, scratches are formed on the surface of the material and the depth of the scratches is obtained by the instrument's longitudinal sensor. The scratch depth can be used to evaluate properties such as hardness, toughness and wear resistance of the material. Typically, a shallow scratch depth means that the material surface has a high degree of hardness, while a deeper scratch depth may mean that the material is less hard and prone to damage or destruction (Liu et al., 2020). Fig. 9 shows the scratch depth–displacement curve obtained from the micro-scratch test. The scratch depth represents the depth of the indenter tip penetrated the sample surface, which is indicative

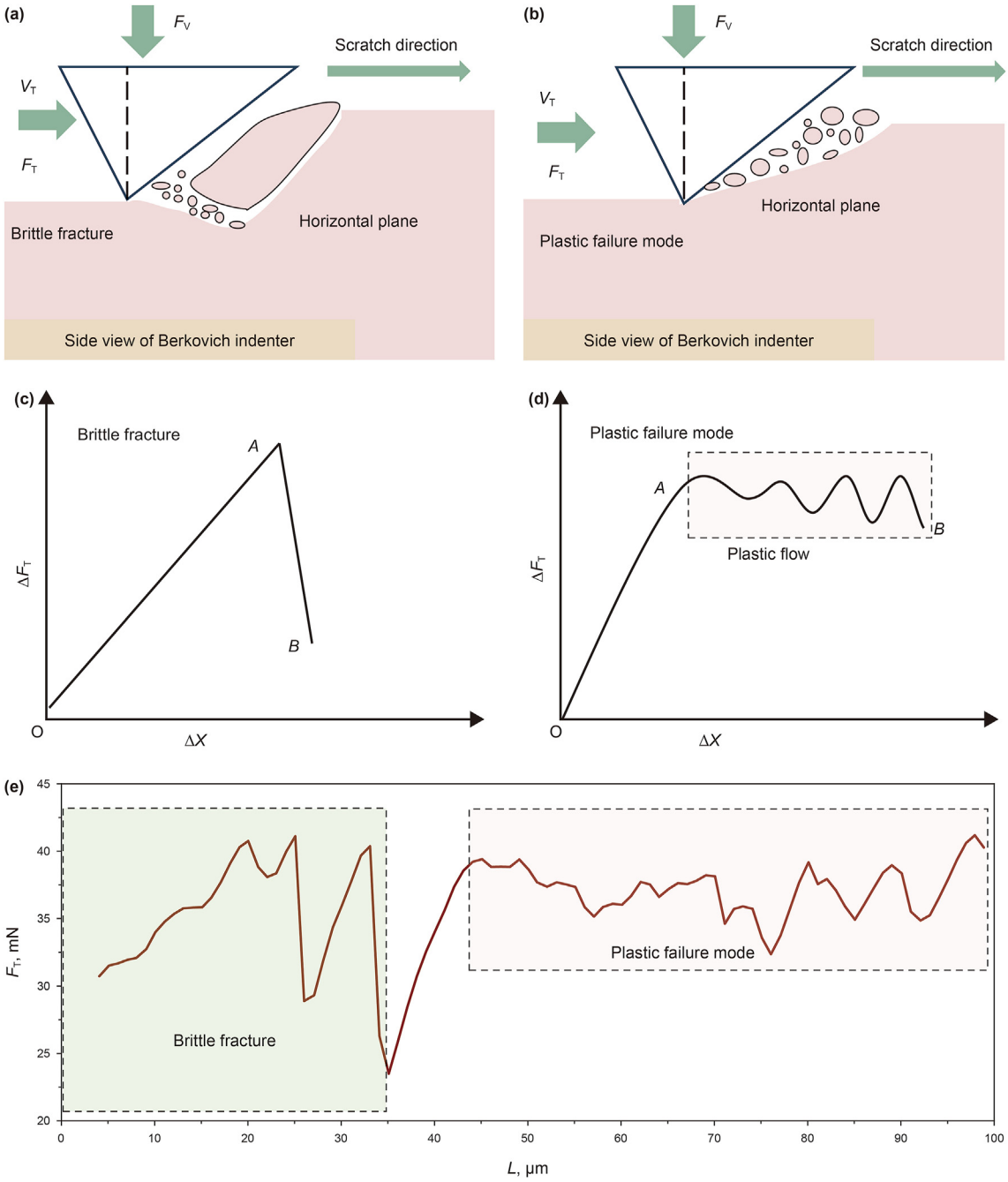


**Fig. 10.** Typical failure mode of shale. (**a**) Brittle failure mode; (**b**) Plastic failure mode; (**c**) Brittle failure curve; (**d**) Plastic failure curve; (**e**) Actual scratch curve.

of the sample's deformation. The greater the deformation, the softer the sample is. The initial scratch curve of the matrix is shown in Fig. 9(a). The maximum scratch depth is 4759.89 nm, and the average scratch depth is 4138.32 nm. The result after 8 days of saturation is shown in Fig. 9(b). The maximum depth of scratch is 5173.52 nm, a 24.37% increase. The average scratch depth is 4180.58 nm, a 1.02% increase. The increased deformation of the matrix indicates that the SCBRIs softens the matrix.

The initial scratch curve of the lamina is shown in Fig. 9(c). The maximum scratch depth is 2501.61 nm, and the average scratch depth is 1899.57 nm. Both the maximum and mean depth for the lamina is smaller than those of the maximum and mean depth for the matrix, indicating that the matrix is softer than the lamina. The results after 8 days of saturation are shown in Fig. 9(d). The maximum scratch depth is 2846.87 nm, a 13.8% increase. The average scratch depth is 2552.66 nm, a 34.38% increase. The increase in both the maximum and average scratch depths of the lamina suggests that SC-$CO_2$–brine interactions reduce the hardness of the lamina. It is noteworthy that the increase in the average depth of the lamina (34.38%) is much larger than the increase in the average depth of the matrix (1.02%). This shows that SCBRIs soften the lamina much greater than the matrix.

### 3.4. Effect of SCBRI on destructive failure mechanisms

The $F_T$–$L$ curves before and after shale saturation are obtained

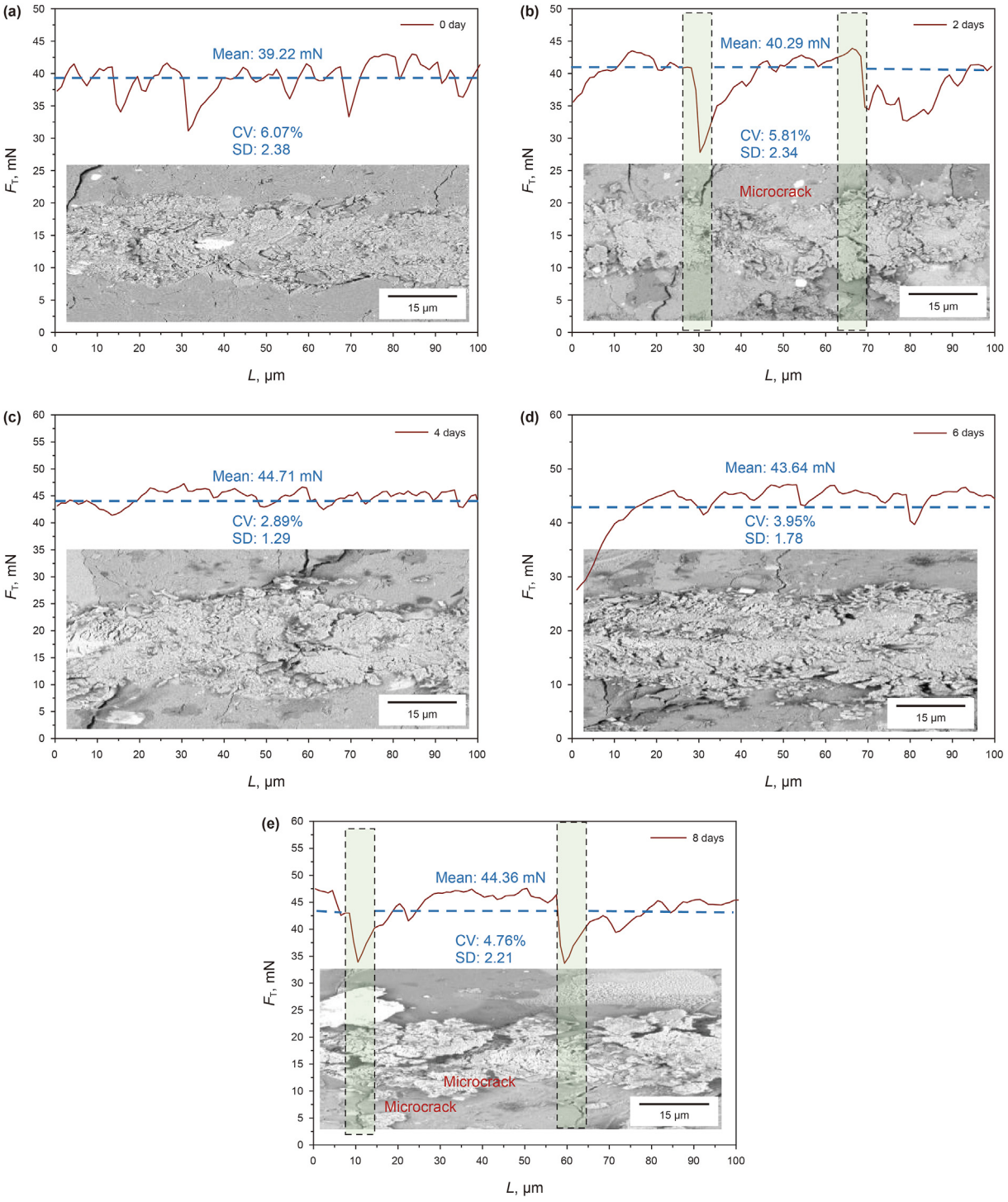


**Fig. 11.** Failure characteristics of matrix destruction at 0 (**a**), 2 (**b**), 4 (**c**), 6 (**d**), 8 (**e**) days of saturation.

following the micro-scratch experiments. As shown in Fig. 10(a), these curves exhibit a pronounced "sawtooth" horizontal force response, which is characteristic of the brittle failure mode. During the scratch process, a macroscopic fracture is produced at the tip of the scratch indenter. This fracture then propagates upwards towards the rock surface in front of the scratch indenter, resulting in the stripping off of larger particles and fragments. A typical curve of the brittle damage mode is shown in Fig. 10(c). The *OA* segment of the curve is linear, representing the elastic deformation regime. However, after reaching the peak point *A*, the horizontal force experiences a sudden drop in the *AB* segment (Akono and Kabir, 2016).

The plastic failure mode is modeled as shown in Fig. 10(b). As the rock matrix and particles are removed by the moving scratch indenter, rock particles continuously accumulate in front of the cutter and are subsequently removed (Richard et al., 2012). A typical curve of the plastic failure mode is shown in Fig. 10(d). The *OA* segment is essentially linear, corresponding to the elastic

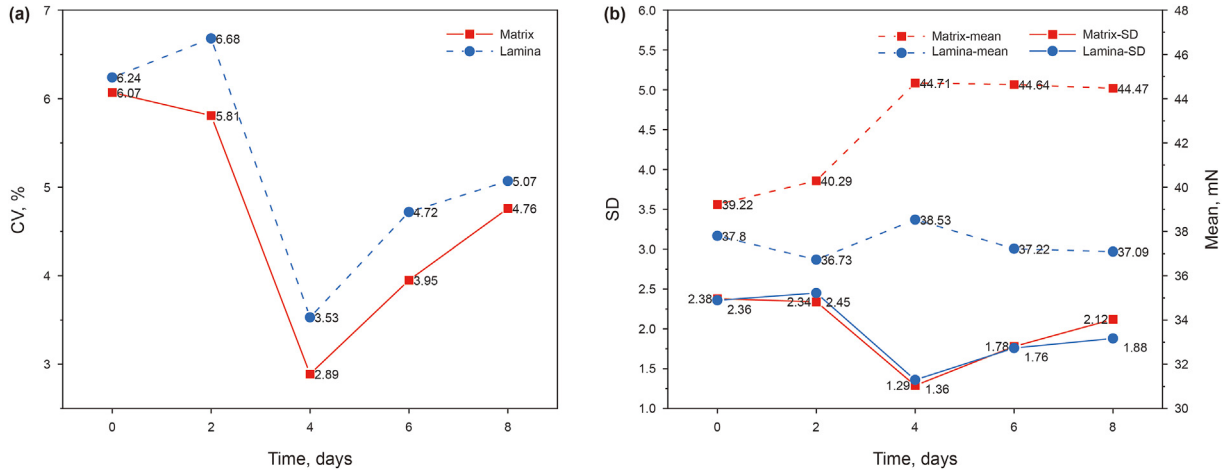


**Fig. 12.** Statistical results of matrix and lamina failure modes at different saturation time. (**a**) CV; (**b**) SD and mean.

deformation. After reaching the peak point *A*, the horizontal force in the *AB* section shows small fluctuation, while the displacement increases continuously. This phenomenon in the *AB* section, where rapid strain energy release is absent, is referred to as "plastic flow" (Kolawole and Ispas, 2020). The morphology of the curves during the actual scratching process is shown in Fig. 10(e). The green dashed portion represents the brittle failure mode, while the red dashed portion represents the plastic failure mode. The fluctuations in the curves for the brittle failure mode are large, whereas the fluctuations for the plastic failure mode are small. However, the responses of the scratch transverse force curves under different conditions are extremely different, making the identification of the curves for brittle failure mode is difficult. In this study, the degree of plastic failure mode in the failure process is determined based on plastic flow. A statistical coefficient of variation (CV) index is introduced to define the degree of plastic failure mode. A larger CV indicates a smaller degree of plastic damage in the rock. The formula for calculating the CV is shown below:

$$\mathrm{CV} = \frac{\sigma}{\bar{x}} \tag{10}$$

$$\sigma = \sqrt{\frac{\sum_{i=1}^{n} (x_i - \bar{x})^2}{n}} \tag{11}$$

where $\sigma$ is the standard deviation; CV is a dimensionless parameter; and $\bar{x}$ is the sample mean.

Fig. 11(a) shows the results of $F_T$–$L$ scratching on the matrix before SC-$CO_2$–brine saturation. The mean, standard deviation, and CV are 39.22 mN, 2.38, and 6.07%, respectively. Fig. 11(e) shows the results of $F_T$–$L$ scratching on the matrix after SC-$CO_2$–brine saturation for 8 days. The mean, standard deviation, and CV are 44.26 mN, 2.21, and 4.76%, respectively. It is worth noting that the horizontal force curves exhibited a sudden drop after the 2nd and 8th day of SC-$CO_2$–brine saturation. This phenomenon is observed in conjunction with SEM, which reveals the presence of microfractures. In order to avoid the error of CV index caused by crack location, the parameters at this location are not considered in the calculation process.

The statistical results of the CV of the matrix at different SC-$CO_2$–brine saturation time are shown in Fig. 12(a). The CV of the matrix shows a tendency to decrease and then increase. However, ultimately, the CV of the matrix decreased by 21.58% after SC-$CO_2$–brine saturation, compared to that before saturation. This indicates that SC-$CO_2$–brine enhances the plastic failure mode of the shale matrix, and this plastic failure also shows a tendency of increasing and then decreasing. The statistical results of the average horizontal force values for the matrix at different SC-$CO_2$–brine saturation time are shown in Fig. 12(b). During the first 4 days of SC-$CO_2$–brine saturation, the average horizontal force of the matrix shows a rapid increase of 14% compared to the initial state. Over the subsequent 4 days of SC-$CO_2$–brine saturation, the change in the average horizontal force of the matrix is a small decrease. The final increase is 13.39% compared to the initial state.

Fig. 13(a) shows the results of $F_T$–$L$ scratching on the lamina before SC-$CO_2$–brine saturation. The mean, standard deviation, and CV are 37.80 mN, 2.36, and 6.24%, respectively. In addition, the results of $F_T$–$L$ scratching on the lamina after SC-$CO_2$–brine saturation for 8 days. The mean, standard deviation, and CV are 37.09 mN, 1.88, and 5.07%, respectively. It is worth noting that the horizontal force of the curve exhibits a sudden drop after 6 and 8 days of the SC-$CO_2$–brine saturation. Combined with SEM analysis, the presence of large hard grains is detected at these locations. On day 6 and day 8, the CV are 12.68% and 13.40%, respectively. In both cases, the CV is larger than 10%, indicating brittle damage. In order to avoid the error of CV index caused by crack location, the parameters at this location are not considered in the calculation process.

The CV values of the lamina under different SC-$CO_2$–brine saturation time are shown in Fig. 12(a). The CV of the lamina shows a tendency to decrease and then increase. However, the CV of the matrix decreased by 18.75% after SC-$CO_2$–brine saturation compared to that before saturation. This fully demonstrates that SC-$CO_2$–brine improves the plastic failure of the lamina. This plastic failure similarly shows an increasing and then decreasing trend. From the statistical results of CV in Fig. 12(a), it is found that the CV of the lamina is larger than that of the matrix, which indicates that the plastic failure of the matrix is larger than that of the lamina. Additionally, the CV of both the matrix and lamina reaches a minimum after 4 days of saturation. The average horizontal force of the lamina after different SC-$CO_2$–brine saturation time are shown in Fig. 12(b), which shows a small fluctuating tendency, and finally decreases by 1.87% compared to the initial state.

### 3.5. Effect of SC-$CO_2$–brine on fracture toughness

The red curve in Fig. 14 shows the fracture toughness of the

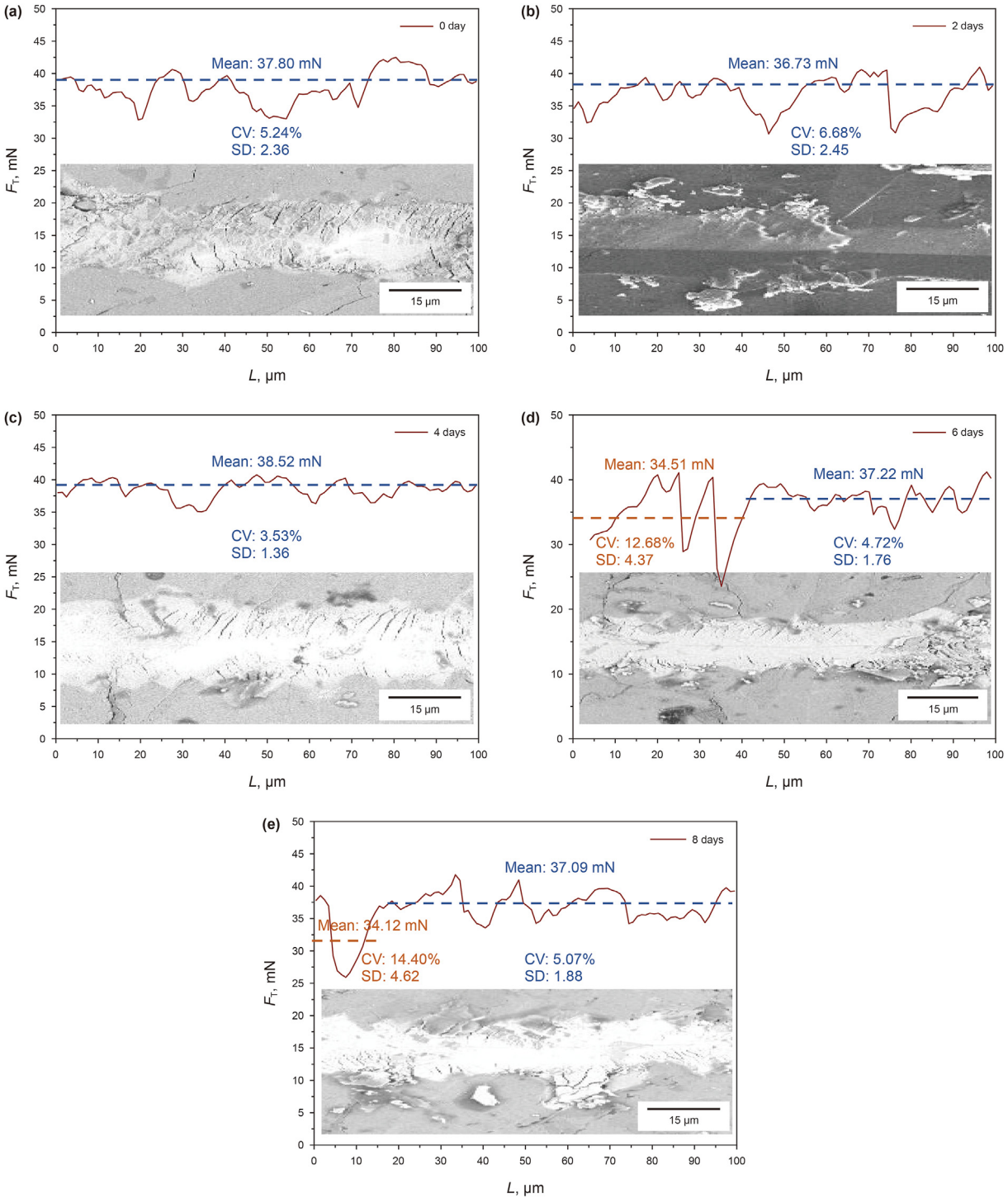


**Fig. 13.** Failure characteristics of the lamina after 0 (**a**), 2 (**b**), 4 (**c**), 6 (**d**), 8 (**e**) days of saturation.

lamina after SC-$CO_2$–brine saturation. The fracture toughness of the lamina exhibits an initial increase followed by a subsequent decrease. Before SC-$CO_2$–brine saturation, the initial average fracture toughness of lamina is 1.92 MPa·$m^{1/2}$. After 2 days of SC-$CO_2$–brine saturation, the average fracture toughness increases to 2.03 MPa·$m^{1/2}$, but then decreases to 1.86 MPa·$m^{1/2}$ after 4 days and further decreases to 1.79 MPa·$m^{1/2}$ after 6 days. The average fracture toughness ultimately decreases to 1.26 MPa·$m^{1/2}$ after 8 days, resulting in a 34.38% reduction. This reduction in fracture toughness of the lamina is attributed to the high permeability and solubility of SC-$CO_2$–brine. The strong penetration of SC-$CO_2$–brine enlarges the microfractures in the lamina, leading to the reduction in fracture toughness. Additionally, the chemical reactions between SC-$CO_2$–brine and carbonate minerals contribute to the decrease in fracture toughness. Furthermore, the initial fracture toughness of the lamina, measuring 1.92 MPa·$m^{1/2}$, exceeds that of the matrix, which is 0.61 MPa·$m^{1/2}$, indicating a higher fracture toughness of the lamina compared to the matrix.

The changes in fracture toughness of the shale matrix after SC-$CO_2$–brine saturation are denoted by the blue curve in Fig. 14. The

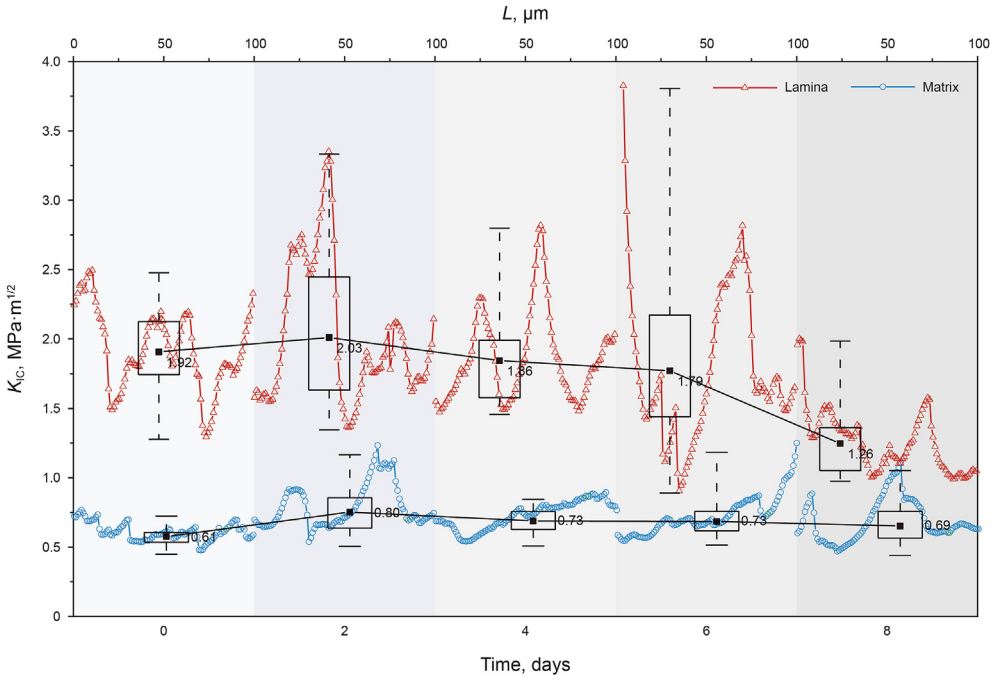


**Fig. 14.** Evolution of lamina and matrix fracture toughness at different saturation time.

general trend of the scratch fracture toughness of the matrix indicates a slight increase after SC-$CO_2$–brine saturation. The initial average fracture toughness measured 0.61 MPa·m$^{1/2}$. Subsequently, the fracture toughness after 2, 4, 6 and 8 days of saturation are 0.80, 0.73, 0.73, and 0.69 MPa·m$^{1/2}$, respectively. The final decrease in fracture toughness amounts to 13.11%. After 2 days of SC-$CO_2$–brine saturation process, the matrix fracture toughness was slightly improved, which may be due to the large difference in mineral distribution in the scratched area. As the indenter falls on more high-strength minerals, the average value of the probe data will rise.

The fracture toughness in the matrix before and after SC-$CO_2$–brine saturation are shown in Fig. 15(a) and (b). Prior to SC-$CO_2$–brine saturation, the frequency distribution of the fracture toughness is normal, and the cumulative frequency curve shows an S-shaped profile. However, after 8 days of SC-$CO_2$–brine saturation, the frequency distribution curve becomes positively skewed, and the cumulative frequency curve adopts a parabolic shape. When the cumulative frequency reaches 50%, the fracture toughness values in the matrix before and after SC-$CO_2$–brine saturation are 0.58 and 0.60 MPa·m$^{1/2}$, respectively. Notably, when the cumulative frequency increases to 64%, after SC-$CO_2$–brine saturation, the fracture toughness is 0.67 MPa·m$^{1/2}$, which is larger than the value at the 90% cumulative frequency prior to SC-$CO_2$–brine saturation. This suggests that a significant increase in the frequency of high fracture toughness measurements, likely due to the indenter contacting some harder minerals. This phenomenon is most likely attributed to the dissolution and precipitation of calcite minerals within the matrix following the SC-$CO_2$–brine saturation process. The large bulk calcite in the matrix dissolved and precipitated into several small fragments, resulting in an increase in the distribution area of calcite. As the scratch indenter traverses the matrix path, the indenter is more likely to encounter a strong mineral such as calcite, which results in increased fracture toughness of the matrix. This observation aligns with the SEM results reported in the previous section. However, it is worth noting that overall, the fracture toughness of the matrix gradually decreases with increasing SC-$CO_2$–brine saturation time, as the dissolution of calcite outweighs the precipitation effect.

The fracture toughness in the lamina before and after SC-$CO_2$–brine saturation is shown in Fig. 15(c) and (d). After 8 days of SC-$CO_2$–brine saturation, the changes in the fracture toughness distribution in the lamina are the same with that in the matrix. Specifically, the distribution curve transforms from a normal to a positively skewed profile, and the cumulative frequency curve shifts from an S-shaped to a parabolic distribution. After an 8-day SC-$CO_2$–brine saturation, the fracture toughness at the 50% cumulative frequency decreases by 39.46%, from 1.12 to 0.68 MPa·m$^{1/2}$. Similarly, the fracture toughness at the 90% cumulative frequency reduces by 34.24%, from 1.44 to 0.95 MPa·m$^{1/2}$. Notably, the fracture toughness at the 98% cumulative frequency after saturation becomes equivalent to the value at the 50% cumulative frequency prior to saturation. These observations indicate a significant reduction in fracture toughness, likely due to the indenter encountering some soft minerals. It is worth noting that the decrease in fracture toughness for both the hard and soft minerals in the lamina before and after saturation is similar. This suggests a uniform softening behavior in the lamina induced by SCBRIs, which is consistent with the SEM results presented in the previous section. Moreover, the softening effect on the lamina is easily influenced by the time of saturation.

## 4. Conclusions

The nanomechanical properties of the shale matrix and lamina are studied, and the mechanical changes over a period of 8 days after SC-$CO_2$–brine saturation are compared. The surface strength, fracture toughness, and deformation properties of the shale are analyzed before and after SC-$CO_2$–brine saturation. Using nanoscratch, scanning electron microscopy (SEM), quantitative evaluation of minerals (QEMSCAN), and X-ray diffraction (XRD) techniques, three types of minerals are identified in the shale matrix and lamina: clay, quartz, and carbonate minerals. The mechanical properties and softening behavior of these minerals are

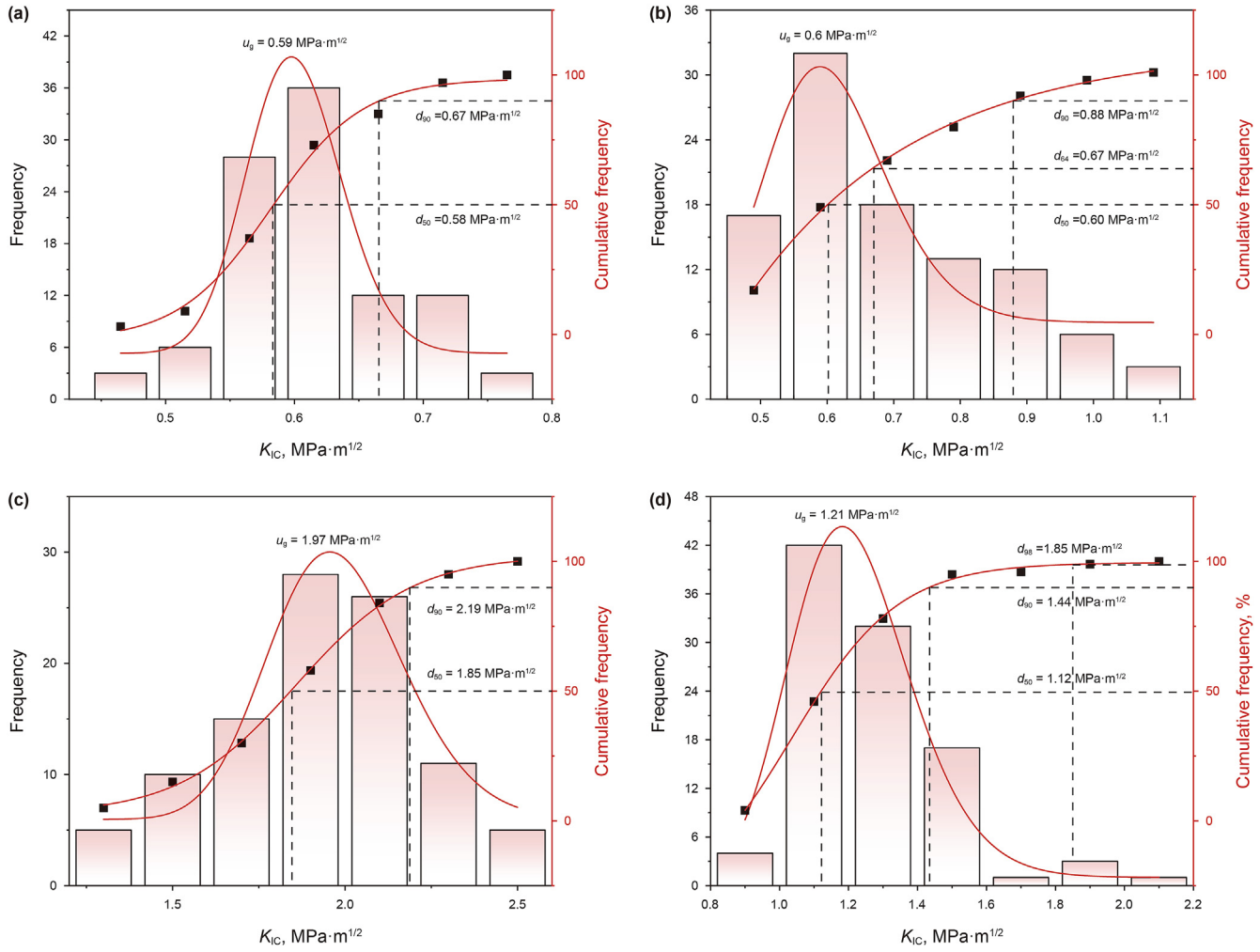


**Fig. 15.** Distribution of fracture toughness in the matrix before (**a**) and after (**b**) SC-$CO_2$–brine saturation and in the lamina before (**c**) and after (**d**) SC-$CO_2$–brine saturation.

characterized before and after SC-$CO_2$–brine saturation. The main findings of this investigation are outlined below.

(1) SEM-QEMSCAN-XRD analysis and micro-scratch results show significant differences in the mineralogy and mechanical properties between the matrix and the lamina. The matrix is found to be abundant in illite, while the lamina is rich in carbonate minerals. The micro-scratch test results show that different damage patterns between the matrix and the lamina. Notably, the through-thickness fractures in the matrix display a finely curved and dispersed distribution, along with wavy interface edges. In contrast, the through-thickness fractures in the lamina are directionally arranged and curved, with smooth and straight interface edges.

(2) The deformation behavior of the shale is altered after SCBRIs. Both the maximum and mean deformations of the shale matrix and lamina show an increasing trend after SC-$CO_2$–brine saturation, indicating a deterioration of their resistance to loads. The maximum deformations increase by up to 24.37% and 13.8% for matrix and lamina, respectively. While the mean deformation increases by up to 1.02% and 34.38% for matrix and lamina, respectively.

(3) With the increase in the SC-$CO_2$–brine interaction time, the degree of plastic failure of matrix and lamina shows a tendency to first increase and then decrease. After SC-$CO_2$–brine saturation, the CV of the lamina and the matrix decreases by 18.75% and 21.58%, respectively. The degree of plastic failure of the matrix is greater than that of the lamina.

(4) With the increase in the SC-$CO_2$–brine interaction time, the fracture toughness of the lamina and the matrix shows a change pattern of increasing and then decreasing. However, the change varies under the same saturation time. Finally, the average fracture toughness of the lamina and the matrix decreases by 34.38% and 13.11%, respectively.

## CRediT authorship contribution statement

**Liu Yang:** Writing – review & editing. **Zhao-Yang Liu:** Writing – original draft. **Yuan-Xun Nie:** Conceptualization. **Zhen-Chuan Han:** Data curation. **Fei Gong:** Supervision. **Ming-Jun Li:** Methodology. **Yan Liu:** Resources.

## Declaration of competing interest

The manuscript has not been published before and is not being considered for publication elsewhere. All authors have contributed to the creation of this manuscript for important intellectual content and read and approved the final manuscript. We declare there is no conflict of interest.

## Acknowledgements

This work is supported by the National Natural Science Foundation of China (52374014) and the Fundamental Research Funds for the Central Universities (2024ZKPYSB03).

## References

Akono, A.T., Kabir, P., 2016. Microscopic fracture characterization of gas shale via scratch testing. Mech. Res. Commun. 78, 86–92. https://doi.org/10.1016/j.mechrescom.2015.12.003.

Akono, A.T., Ulm, F.-J., 2017. Microscopic toughness of viscous solids via scratching: from amorphous polymers to gas shale. J. Nanomech. Micromech 7 (3), 04017009. https://doi.org/10.1061/(asce)nm.2153-5477.0000131.

Akono, A.T., Reis, P.M., Ulm, F.J., 2011. Scratching as a fracture process: from butter to steel. Phys. Rev. Lett. 106 (20), 204302. https://doi.org/10.1103/PhysRevLett.106.204302.

Bai, B., Ni, H.-j., Shi, X., Guo, X., Ding, L., 2021. The experimental investigation of effect of supercritical $CO_2$ immersion on mechanical properties and pore structure of shale. Energy 228, 120663. https://doi.org/10.1016/j.energy.2021.120663.

Bandini, A., Paolo, B., Bemporad, E., Sebastiani, M., Chicot, D., 2014. Role of grain boundaries and micro-defects on the mechanical response of a crystalline rock at multiscale. Int. J. Rock Mech. Min. 71, 429–441. https://doi.org/10.1016/j.ijrmms.2014.07.015.

Bull, S.J., 1997. Failure mode maps in the thin film scrach adhesion test. Tribol. Int. 30, 491–498. https://doi.org/10.1016/S0301-679X(97)00012-1.

Cheng, Y.G., Zeng, M.R., Lu, Z.H., Du, X.D., 2020. Effects of supercritical $CO_2$ treatment temperatures on mineral composition, pore structure and functional groups of shale: implications for $CO_2$ sequestration. Sustainability-Basel 12 (9), 3927. https://doi.org/10.3390/su12093927.

Espinoza, D.N., Kim, S.H., Santamarina, J.C., 2011. $CO_2$ geological storage—geotechnical implications. KSCE J. Civ. Eng. 15 (4), 707–719. https://doi.org/10.1007/s12205-011-0011-9.

Fan, M., Jin, Y., Chen, M., Geng, Z., 2019. Mechanical characterization of shale t-through instrumented indentation test. J. Petrol. Sci. Eng. 174, 607–616. https://doi.org/10.1016/j.petrol.2018.11.083.

Fatah, A., Bennour, Z., Mahmud, H.B., Gholami, R., Hossain, M., 2021. Surface wettability alteration of shales exposed to $CO_2$: implication for long-term integr-ity of geological storage sites. Int. J. Greenh. Gas Con. 110, 103426. https://doi.org/10.1016/j.ijggc.2021.103426.

Golovin, Y.I., Tyurin, A.I., Victorov, S.D., Kochanov, A.N., Pirozhkova, T.S., 2018. Size effects and charting the physical and mechanical properties of individual phases and interphases in polycrystalline materials. Bull. Russ. Acad. Sci. Phys. 82 (7), 856–859. https://doi.org/10.3103/s1062873818070201.

Goodman, A., Sanguinito, S., Tkach, M., Natesakhawat, S., Kutchko, B., 2019. Investigating the role of water on $CO_2$-Utica Shale interactions for carbon storage and shale gas extraction activities – evidence for pore scale alterations. Fuel 242, 744–755. https://doi.org/10.1016/j.fuel.2019.01.091.

Heng, S., Li, X., Liu, X., Chen, Y., 2020. Experimental study on the mechanical properties of bedding planes in shale. J. Nat. Gas Sci. Eng. 76, 103161. https://doi.org/10.1016/j.jngse.2020.103161.

Kolawole, O., Ispas, I., 2020. Evaluation of geomechanical properties via scratch tests: where are we and where do we go from here? SN Appl. Sci. 2 (10), 1633. https://doi.org/10.1007/s42452-020-03469-5.

Li, C., Ostadhassan, M., Guo, S., Gentzis, T., Kong, L., 2018. Application of peak force tapping mode of atomic force microscope to characterize nanomechanical properties of organic matter of the Bakken Shale. Fuel 233, 894–910. https://doi.org/10.1016/j.fuel.2018.06.021.

Li, Y., Chen, J.Q., Yang, J.H., Liu, J.S., Tong, W.S., 2022. Determination of shale macroscale modulus based on microscale measurement: a case study concerning multiscale mechanical characteristics. Petrol. Sci. 19 (3), 1262–1275. https://doi.org/10.1016/j.petsci.2021.10.004.

Liu, A., Liu, S., Liu, Y., Liu, B., Liu, T., 2022. Characterizing mechanical heterogeneity of coal at nano-to-micro scale using combined nanoindentation and FE-SEM-EDS. Int. J. Coal Geol. 261. https://doi.org/10.1016/j.coal.2022.104081.

Liu, J., Zeng, Q., Xu, S., 2020. The state of art in characterizing the micro/nano-structure and mechanical properties of cement-based materials via scratch test. Construct. Build. Mater. 254. https://doi.org/10.1016/j.conbuildmat.2020.119255.

Liu, K., Jin, Z.J., Zakharova, N., Zeng, L.B., Haghshenas, M., Adeyilola, A., 2023a. Comparison of shale fracture toughness obtained from scratch test and nano-indentation test. Int. J. Rock Mech. Min. 162, 1005282. https://doi.org/10.1016/j.ijrmms.2022.105282.

Liu, K., Jin, Z.J., Zeng, L.B., Ozotta, O., Gentzis, T., Ostadhassan, M., 2023b. Alteration in the mechanical properties of the Bakken during exposure to supercritical $CO_2$. Energy 262, 125545. https://doi.org/10.1016/j.energy.2022.125545.

Liu, M., Hou, D., Wang, Y., Lakshminarayana, G., 2023. Micromechanical properties of $Dy^{3+}$ ion-doped $(Lu_xY_{1-x})_3Al^5O_{12}$ ($x$ = 0, 1/3, 1/2) single crystals by indentation and scratch tests. Ceram. Int. 49 (3), 4482–4504. https://doi.org/10.1016/j.ceramint.2022.09.334.

Liu, Y., Liu, A., Liu, S., Kang, Y., 2022. Nano-scale mechanical properties of constituent minerals in shales investigated by combined nanoindentation statistical analyses and SEM-EDS-XRD techniques. Int. J. Rock Mech. Min. 159, 105187. https://doi.org/10.1016/j.ijrmms.2022.105187.

Lu, J., Nicot J, P., Mickler, P.J., Ribeiro, L.H., Darvari, R., 2016. Alteration of Bakken reservoir rock during $CO_2$-based fracturing—an autoclave reaction experiment. Journal of Unconventional Oil and Gas Resources 14, 72–85. https://doi.org/10.1016/j.juogr.2016.03.002.

Luo, X., Ren, X., Wang, S., 2019. Supercritical $CO_2$-water-shale interactions and their effects on element mobilization and shale pore structure during stimulation. Int. J. Coal Geol. 202, 109–127. https://doi.org/10.1016/j.coal.2018.12.007.

Middleton, R., Viswanathan, H., Currier, R., Gupta, R., 2014. $CO_2$ as a fracturing fluid: potential for commercial-scale shale gas production and $CO_2$ sequestration. Energy Proc. 63, 7780–7784. https://doi.org/10.1016/j.egypro.2014.11.812.

Nie, Y.X., Zhang, G.Q., Wen, J., Li, S., Zhou, D., 2022. Microscale damage induced by $CO_2$ storage on the microstructure of sandstone coupling hydro-–mechanical–chemical processes. Energy & Fuels. 36 (24), 15023–15036. https://doi.org/10.1021/acs.energyfuels.2c03131.

Nie, Y.X., Wu, B.S., Zhang, G.Q., Zhang, L., Li, S.Y., Yang, L., Liu, Z.Y., 2024. Determination of the thickness and fracture toughness of shale interfacial transition zone near various micromineral aggregates using nano-scratch tests. SPE J. 29 (5), 2414–2431. https://doi.org/10.2118/219470-PA.

Osborn, S.G., Vengosh, A., Warner, N.R., Jackson, R.B., 2011. Methane contamination of drinking water accompanying gas-well drilling and hydraulic fracturing. Proc. Natl. Acad. Sci. USA 108 (20), 8172–8176. https://doi.org/10.1073/pnas.1100682108.

Richard, T., Dagrain, F., Poyol, E., Detournay, E., 2012. Rock strength determination from scratch tests. Eng. Geol. 147–148, 91–100. https://doi.org/10.1016/j.enggeo.2012.07.011.

Shi, X., Jiang, S., Wang, Z.X., Bai, B., Xiao, D.S., Tang, M.M., 2020. Application of nanoindentation technology for characterizing the mechanical properties of shale before and after supercritical $CO_2$ fluid treatment. J. $CO_2$ Util. 37, 158–172. https://doi.org/10.1016/j.jcou.2019.11.022.

Stavropoulou, E., Laloui, L., 2022. Insights into the interaction of a shale with $CO_2$. Solid Earth 13 (12), 1823–1841. https://doi.org/10.5194/se-13-1823-2022.

Tan, J., Xie, B., Lyu, Q., Chen, S., Ranjith, P.G., 2022. Mechanical properties of shale after $CO_2$ and $CO_2$-based fluids imbibition: experimental and modeling study. Rock Mech. Rock Eng. 55 (3), 1197–1212. https://doi.org/10.1007/s00603-021-02702-w.

Tao, J.P., Meng, S.W., Li, D.X., Cao, G., Gao, Y., Liu, H., 2022. Experimental study on the impact of $CO_2$ treatment on different lithofacies in shale oil reservoirs. Appl. Sci. 12 (4), 2217. https://doi.org/10.3390/app12042217.

Veytskin, Y.B., Tammina, V.K., Bobko, C.P., Hartley, P.G., Clennell, M.B., Dewhurst, D.N., Dagastine, R., 2017. Micromechanical characterization of shales through nanoindentation and energy dispersive X-ray spectrometry. Geomech. Energy Envir. 9, 21–35. https://doi.org/10.1016/j.gete.2016.10.004.

Wang, X., Alvarado, V., Swoboda-Colberg, N., Kaszuba, J.P., 2013. Reactivity of dolomite in water-saturated supercritical carbon dioxide: significance for carbon capture and storage and for enhanced oil and gas recovery. Energy Convers. Manag. 65, 564–573. https://doi.org/10.1016/j.enconman.2012.07.024.

Wei, Y., Kong, W., Wang, Y., Sha, A., 2021. Multifunctional application of nanoscratch technique to characterize cementitious materials. Cement Concr. Res. 140, 106318. https://doi.org/10.1016/j.cemconres.2020.106318.

Wu, S., Ge, H.K., Li, T.T., Wang, X.Q., Li, N., Zou, Y.S., Gao, K., 2022. Characteristics of fractures stimulated by supercritical carbon dioxide fracturing in shale based on acoustic emission monitoring. Int. J. Rock Mech. Min. 152, 105065. https://doi.org/10.1016/j.ijrmms.2022.105065.

Yang, K., Zhou, J.P., Xian, X.F., Zhang, C.P., Gan, Q., Dong, Z.Q., 2023. Effect of supercritical $CO_2$-water-shale interaction on mechanical properties of shale and its implication for carbon sequestration. J. Nat. Gas Sci. Eng. 111, 204930. https://doi.org/10.1016/j.jgsce.2023.204930.

Yang, L., Wang, H., Xu, H., Guo, D., Li, M., 2023. Experimental study on characteristics of water imbibition and ion diffusion in shale reservoirs. J. Petrol. Sci. Eng. 229, 212167. https://doi.org/10.1016/j.geoen.2023.212167.

Yang, L., Yang, D., Li, Y., Cai, J., Jiang, X., 2024. Nanoindentation study on microscopic mineral mechanics and bedding characteristics of continental shales. Energy. https://doi.org/10.2139/ssrn.4712842.

Zhang, Y., Lashgari, H.R., Sepehrnoori, K., Di, Y., 2017. Effect of capillary pressure and salinity on $CO_2$ solubility in brine aquifers. Int. J. Greenh. Gas Control 57, 26–33. https://doi.org/10.1016/j.ijggc.2016.12.012.

Zhou, J., Tian, S.F., Zhou, L., Xian, X.F., Zhang, C.P., Yang, K., Dong, Z.Q., Lu, Z.H., 2021. Effect of sub-/super-critical $CO_2$ and brine exposure on the mechanical and acoustic emission characteristics of shale. J. Nat. Gas Sci. Eng. 90, 103921. https://doi.org/10.1016/j.jngse.2021.103921.